A three-electrode integrated photo-supercapacitor utilizing graphene-based intermediate bifunctional electrode

S.C. Lau[a], H.N. Lim[a,b,*], T.B.S.A. Ravoof[a], M.H. Yaacob[c], D.M. Grant[d], R.C.I. MacKenzie[d], I. Harrison[e], N.M. Huang[f]

[a] Department of Chemistry, Faculty of Science, Universiti Putra Malaysia, 43400 UPM Serdang, Selangor, Malaysia
[b] Institute of Advanced Technology, University Putra Malaysia, 43400 UPM Serdang, Selangor, Malaysia
[c] Wireless and Photonics Network Research Centre, Universiti Putra Malaysia, 43400 UPM Serdang, Selangor, Malaysia
[d] Advanced Materials Research Group, Faculty of Engineering, University of Nottingham, Nottingham NG7 2RD, United Kingdom
[e] Department of Electrical and Electronic Engineering, Faculty of Engineering, University of Nottingham, Nottingham NG7 2RD, United Kingdom
[f] Faculty of Engineering, Xiamen University of Malaysia, Jalan Sunsuria, Bandar Sunsuria, 43900 Sepang, Selangor Darul Ehsan, Malaysia

ABSTRACT

A dye-sensitized solar cell (DSSC) employing a compact and mesoporous titania (TiO_2) film as the anode was integrated with a symmetrical supercapacitor utilizing polypyrrole/reduced graphene oxide (PPy/rGO) electrodes to form a photo-supercapacitor. The double-sided-electrodeposited PPy/rGO material served as an intermediate electrode which was bifunctional in nature; acting as a counter electrode for the DSSC to permit electrolyte regeneration, and also as an electrode for the supercapacitor. The isolated DSSC and supercapacitor were characterized before the integration, and the power conversion efficiency (PCE) of the DSSC was 2.4%, while the specific capacitance of the supercapacitor was 308.1 F/g. The performance of the integrated photo-supercapacitor was tested under a light illumination of 100 mW/cm^2. By using a single PPy/rGO electrode at the cell/supercapacitor interface, an extended lifetime was achieved with up to 50 charge/discharge cycles. The photo-supercapacitor possessed a specific capacitance of 124.7 F g^{-1}, and a retention percentage of 70.9% was obtained after 50 consecutive charge/discharge cycles.

© 2017 Elsevier Ltd. All rights reserved.

1. Introduction

Solar energy conversion and electric energy storage have been the subject of much research interest to solve the current energy crisis, in order to cope with the increasing energy demands in our daily lives and the large energy consumption of the industrial sectors [1,2]. DSSCs have attracted much attention in the photovoltaic market because they are relatively simple and low-cost fabrication method compared to a conventional silicon solar device [3–6] with promising efficiency and good stability [7,8]. The archetypical DSSC is composed of a dye-sensitized mesoporous metal oxide film as the photoanode, a triiodide/iodide redox couple as the electrolyte, and a platinum counter electrode [3,5,9]. In this work, nano-sized TiO_2 was employed as the photoanode material because it provides a large surface area for effective dye absorption and has suitable pore sizes for electrolyte diffusion [10,11].

Although sunlight is a promising source of renewable energy, technology to store the harvested energy for use during darkness is required for the full transition to renewable energy [12,13]. Supercapacitors or ultracapacitors, are currently the focus of considerable academic and industrial research because of their relatively long cycle-life, high power and energy densities, simple charging principles, fast charge-discharge processes, and maintenance-free operation [14–16]. Graphene is a suitable material for electric double-layer capacitors (EDLC) as it has a high electrical and thermal conductivity up to $5000 \, W \, m^{-1} \, K^{-1}$, a large surface area of $2630 \, m^2 \, g^{-1}$, and is capable of ultra-high electron mobility of $200 \, 000 \, cm^2 \, V^{-1} \, s^{-1}$, is relatively low cost, and has a good intrinsic capacitance performance of $21 \, \mu F \, cm^{-2}$ [15,17].

Currently, to use harvested solar energy for useful work during the night, a combined system that includes a solar cell and energy storage unit is employed, which can be integrated into a single device [18–20]. The integrated photo-supercapacitor would need

* Corresponding author at: Department of Chemistry, Faculty of Science, Universiti Putra Malaysia, 43400 UPM Serdang, Selangor, Malaysia.
E-mail address: janetlimhn@gmail.com (H.N. Lim).

to be lightweight and portable [18,20]. In this work, a graphene-based hybrid electric double-layer capacitor (hEDLC) was employed as the intermediate electrode in a three-electrode photo-supercapacitor to further enhance the life time and stability of the integrated device. By using the graphene-based interlayer, we demonstrate up to 50 charge-discharge cycles, and a charge retention of 70.9%. The ability to generate power and to store energy in a single device, offers a potential route to, renewable, all day and all night, low carbon electricity.

Fig. 1 shows the configuration of a three-electrode photo-supercapacitor, which includes sandwiched multi-layered electrodes made up of a dye-sensitized TiO_2 nanoparticles-based photo-anode (positive electrode) and polypyrrole/reduced graphene oxide (PPy/rGO) in contact with the iodolyte, and two PPy/rGO electrodes in contact with the hydrogel electrolyte. The intermediate PPy/rGO electrodes are bifunctional in nature, acting as a counter electrode to permit electrolyte regeneration for the DSSC on one side, and as charge storage for the supercapacitor on the other side [12,21,22]. Two electrolytes work simultaneously on each side [8]. The bottom-most PPy/rGO electrode acts as a negative electrode. This interesting design of a photo-super-capacitor where a graphite sheet is directly utilized as the current collector with PPy/rGO deposited on both its surfaces, provides conducting channels and promotes the maximum electrochemical utilization of the PPy pseudo-capacitance [25]. Three-electrode configured photo-supercapacitors have been reported to exhibit a high maximum voltage, which results in a high energy and power density, small voltage drop, high power conversion efficiency (PCE), high charge/discharge durability, and long lifetimes [8,21,22].

2. Experimental Methods

2.1. Materials

Titanium (IV) tetraisopropoxide (TTIP >98%), titanium (IV) oxide (P25) powder, and pyrrole (99%) were purchased from Acros Organics. N3 dye (Ruthenizer 535-bisTBA) and the redox electrolyte (Iodolyte Z-100) were obtained from Solaronix. Indium tin oxide (ITO) conducting glass slides ($7\,\Omega\,sq^{-1}$) were purchased from Xin Yan Technology Limited, China. Potassium hydroxide (KOH, 85%) was purchased from Hamburg Chemicals. Sodium p-toluenesulfonate (NapTS), polyvinyl alcohol (PVA) flakes (MW ∼60 000), and glycerol were purchased from Merck.

2.2. Fabrication of the dye-sensitized solar cells

The photoanode was prepared by cleaning the ITO conductive glass via sonication using acetone, methanol, and deionized water three times for 5 min each. Subsequently, a TiO_2 compact layer with an active surface area of 1.0 cm × 1.0 cm was deposited onto the cleaned ITO glass using aerosol-assisted chemical vapor deposition (AACVD) at 400 °C for 30 min. A 0.1 M TTIP solution in 50 ml of toluene was used to generate an aerosol with an air humidifier, and argon gas was allowed to flow through the reaction chamber at a flow rate of $300\,mL\,min^{-1}$. The reaction was carried out in a fumehood. After the deposition, the substrate was allowed to cool to room temperature. Then, TiO_2 paste was prepared by dissolving 1.60 g of P25 in 8 ml of ethanol. The mixture was stirred for 5 min followed by the addition of 0.10 M TTIP with continual stirring. The mixture was then horn-sonicated for 30 min to obtain a well-dispersed paste. The paste was coated on an ITO substrate using the doctor's blade method and sintered at 400 °C for 15 min to enhance the adhesion of the paste onto the substrate. After the sintering process, the ITO substrate was immersed in 0.3 mM of N3 dye for 24 h in dark conditions. After the dye-sensitization process, the ITO substrate was washed with ethanol to remove any excess dye, and the photoanode was produced.

The preparation of the PPy/rGO counter electrode was carried out by dissolving 0.1 M NapTS in $1\,mg\,ml^{-1}$ of GO solution (prepared using the simplified Hummer's method [26]). NapTS was used as a dopant and supporting electrolyte for depositing the polypyrrole membranes [27]. The mixture was stirred for 5 min before the addition of 0.1 M of pyrrole. The mixture was stirred again until a homogenous solution was obtained. An electrochemical analyzer (Versa STAT 3, Princeton Applied Research) was used to electropotentiostatically deposit the PPy/rGO nanocomposite onto the ITO working electrode. A platinum rod was the counter electrode, and an Ag/AgCl electrode was the reference electrode. The deposition was carried out at +0.8 V for 100 s. The ITO substrate was allowed to air-dry, and a solar counter electrode was formed.

The dye-sensitized TiO_2 photoanode was clamped together with the PPy/rGO counter electrode. Then, redox electrolyte was dropped and diffused throughout the active surface between the two electrodes. This DSSC was then used for characterization.

2.3. Fabrication of the PPy/rGO-based supercapacitor

For the preparation of the PPy/rGO electrode material, 0.1 M NapTS was dissolved in $1\,mg\,ml^{-1}$ of GO solution and stirred for
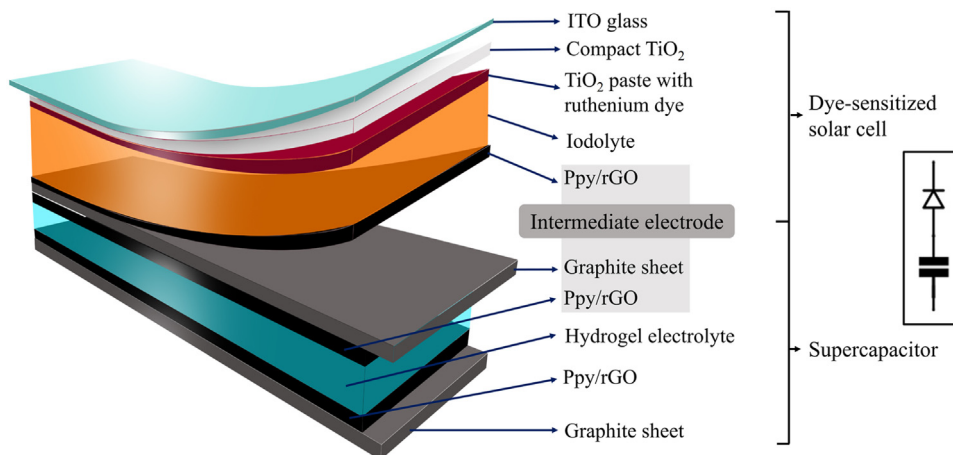
Fig. 1. Device configuration of the three-electrode photo-supercapacitor which consists of a dye-sensitized solar cell (DSSC) and a symmetrical PPy/rGO-based supercapacitor, where both the DSSC and supercapacitor share a common PPy/rGO electrode. A corresponding circuit diagram is shown in the inset.

5 min before the addition of a solution of 0.1 M pyrrole. The mixture was continually stirred until a homogenous solution was obtained. An electrochemical analyzer (Versa STAT 3, Princeton Applied Research) was used to electropotentiostatically deposit the PPy/rGO nanocomposite on a graphite sheet working electrode. A platinum rod was the counter electrode, and an Ag/AgCl electrode was the reference electrode. The deposition was carried out at +0.8 V for 15 min. The graphite sheet substrate was allowed to air-dry. In order to prepare the PVA/KOH hydrogel, 0.1 g ml^{-1} of PVA was added to deionized water and stirred while heating until the mixture turned colorless followed by the addition of 3 M KOH pellets while stirring. Glycerin was finally added to the reaction medium at a 1:10 volume ratio and stirred until a homogeneous, viscous solution was obtained which was poured into a petri dish and left to air-dry overnight. Thus, the PVA/KOH hydrogel polymer electrolyte was successfully formed. The assembly of the supercapacitor was done by sandwiching the as-prepared PVA/KOH hydrogel between two PPy/rGO-based graphite electrodes, which were then compressed using a swage lock device until a maximum contact between the electrodes and hydrogel was obtained.

2.4. Integration of the photo-supercapacitor

The as-prepared photoanode (see Section 2.2) was clamped together with the supercapacitor prepared in Section 2.3. However, for the preparation of the intermediate PPy/rGO electrode materials, the method used was slightly different from that in section 2.3. After 15 min of deposition, the graphite sheet was rotated 180° vertically and deposition was carried out for a further 10 min. This step was taken to ensure that the surface of the graphite sheet facing the hydrogel electrolyte and that facing the iodolyte had the optimum deposition times of 15 min and 10 min, respectively for PPy/rGO materials. The graphite sheet substrate was then allowed to air-dry and the redox electrolyte was subsequently diffused into the photoactive layer. Thus, the integrated photo-supercapacitor was then characterized using a variety of techniques outlined in Section 2.5.

2.5. Characterization Techniques

2.5.1. FESEM
The morphology of the photoanode surfaces with and without TiO$_2$ paste were characterized using field emission scanning electron microscopy (FESEM, FEI Nova Nano SEM 400) under magnifications of 200000× and 60000×, respectively.

2.5.2. Electrochemical measurements
The photovoltaic performance of the DSSC was recorded using an electrochemical analyzer (Versa STAT 3, Princeton Applied Research), under solar illumination from a 150-W xenon arc lamp, with the use of an AM 1.5 G filter. The electrochemical properties of the supercapacitor and photo-supercapacitor were examined using the same electrochemical analyzer. For the supercapacitor, cyclic voltammetry (CV), galvanostatic charge/discharge (GCD), and electrochemical impedance spectroscopy (EIS) were carried out using a swage lock device as a two-electrode system. CV was performed at a working potential of 0–1 V with scan rates of 2–100 mV s^{-1}. The GCD of the two-electrode system was carried out from 0 to 1 V, and the specific capacitance (C$_s$) in F g^{-1} was calculated from the discharge curve using Eq. (1) [28–30].

$$C_s = (i \times \Delta t)/(\Delta V \times m) \qquad (1)$$

where i = constant current during discharge segment (A), Δt = discharge duration (s), ΔV = potential window (V), and m = mass of active material (g). The energy density in Wh kg^{-1} and power

density in W kg^{-1} of the supercapacitor were obtained from Eqs. (2) and (3), respectively [15,30].

$$E_{cell} = (1/2)\left(C_{cell}V^2\right) \times (1000/3600) \qquad (2)$$

$$P_{cell} = (E_{cell}/t) \times 1000 \qquad (3)$$

where C_{cell} = specific capacitance of the cell (F g^{-1}), V = potential window of discharge (V), and t = discharge time (s). EIS was performed between 10 mHz and 100 kHz with an AC amplitude of 5 mV. For the photo-supercapacitor, GCD was performed using a free-standing integrated device, and it was carried out at potential differences of 0.3 V, 0.4 V, and 0.5 V.

3. Results and Discussion

The J-V curves of the different photoanode materials are shown in Fig. 2. The DSSC with only a compact layer exhibited negligible photocurrent. This was due to the very small amount of dye absorbed within the layer after 24 h of dye sensitization. In addition, the dye sensitizer could not thoroughly diffuse through the compact TiO$_2$ layer. The DSSC with only the TiO$_2$ paste without the sintering process only generated slightly less photocurrent than its sintered layer, and both exhibited PCE values of 1.5%. The data obtained showed that the TiO$_2$ paste possessed a mesoporous structure that the dye molecules could diffuse into. After sintering at 400 °C, the paste had stronger adherence to the ITO glass, which would increase the efficiency. In addition, with the deposition of the TiO$_2$ paste on top of the compact layer, followed by the sintering process, the efficiency was improved to 2.4%, with J$_{sc}$ = 7.03 mA cm^{-2}, V$_{oc}$ = 1.0 V, and FF = 0.3406. This verified the role of the compact layer as a blocking agent to decrease the recombination rate of excited electrons. Moreover, since the compact layer was deposited on the ITO at 400 °C, the TiO$_2$ paste effectively adhered to the relatively rough surface of the compact layer compared to the ITO surface (Fig. S1, Supplementary Information). Hence, with the additional calcination, the deposited TiO$_2$ paste showed enhanced adhesion. In this work, the calcination temperature for the TiO$_2$ paste was set to 400 °C, which was lower than other reported values of 450 °C to 500 °C. This was because a few attempts were made with different
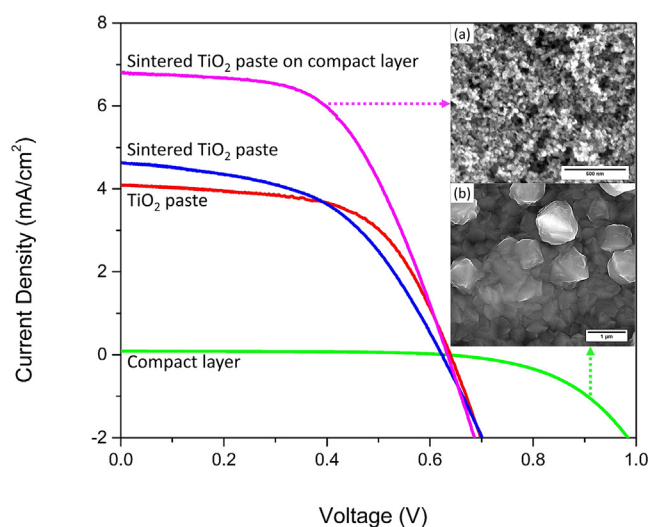
Fig. 2. J-V curves of different photoanode materials, with insets showing FESEM images of (a) TiO$_2$ paste deposited onto the TiO$_2$ compact layer and (b) TiO$_2$ compact layer.

sintering temperatures but no significant changes in device efficiency were observed, in temperatures ranging from 400 °C to 500 °C. The morphology of the TiO_2 compact layers with and without the TiO_2 paste are shown in Fig. 2 insets (a) and (b), respectively. (a) indicated the deposition of the TiO_2 paste onto the compact layer, with nanoparticle sizes of less than 16 nm, and porous spaces between particles of approximately 20–50 nm. This highly porous feature is one of the most important characteristics of the photoanode in the DSSC in order to promote effective dye absorption. In contrast, (b) shows that the titania possessed a compact structure with negligible space between the particles.

The electrochemical capacitance properties of the as-prepared supercapacitor were examined using CV, GCD, and EIS techniques in a two-electrode system. Fig. 3(a) shows the CV curves of the supercapacitor at different scan rates. At scan rates of $100\,mV\,s^{-1}$, $50\,mV\,s^{-1}$, and $10\,mV\,s^{-1}$, there were broad peaks at around 0.4 V, which indicated pseudocapacitance [1]. In addition, the large area under the CV curves indicate a good capacitance value of up to $547.1\,F\,g^{-1}$ at a scan rate of $2\,mV\,s^{-1}$. As the scan rate increased, the peak current increased with the broadening of CV peaks, which was a sign of pseudocapacitance [28]. The asymmetric and non-rectangular shape of the CV curves deviated from typical EDLC properties, and the absence of a pair of redox peaks suggested the combined contribution of the EDLC and pseudo-capacitor to the overall capacitance [25,28,31]. The shapes of all the CV curves in

this work remained similar despite different scan rates, demonstrating good capacitive behavior [29].

The capacitance performance of the PPy/rGO-based super-capacitor was further examined using a GCD test at current densities of $1\,A\,g^{-1}$–$5\,A\,g^{-1}$, and the curves are displayed in Fig. 3(b). All of the curves had nonlinear lines with non-triangular shapes, which confirmed the pseudo-capacitive behavior [28]. All the discharge curves were also obviously divided into two lines with different slopes. In the first section of the curve at a higher potential, the efficient adsorption and desorption of electrolyte ions onto the surface of the active material occurred and resulted in EDLC capacitance. The second section of the discharge curve indicated that a redox-related reaction had occurred [32]. Therefore, the GCD test proved that the specific capacitance of the PPy/rGO-based supercapacitor resulted from the EDLC and pseudo-capacitance combination. The specific capacitance obtained from the GCD decreased as the current density increased (Fig. S2, Supplementary Information). The specific capacitances of the PPy/rGO-based supercapacitor calculated at current densities of 1, 2, 3, 4, and $5\,A\,g^{-1}$ were 308.1, 277.6, 227.2, 222.5, and $225.1\,F\,g^{-1}$ respectively. The gradual decrease in specific capacitance was due to the limited charge/discharge rate of the porous carbon materials [22]. The highest values for energy density and power density calculated at a current density of $1\,A\,g^{-1}$ were $26.6\,Wh\,kg^{-1}$ and $219.1\,W\,kg^{-1}$, respectively.
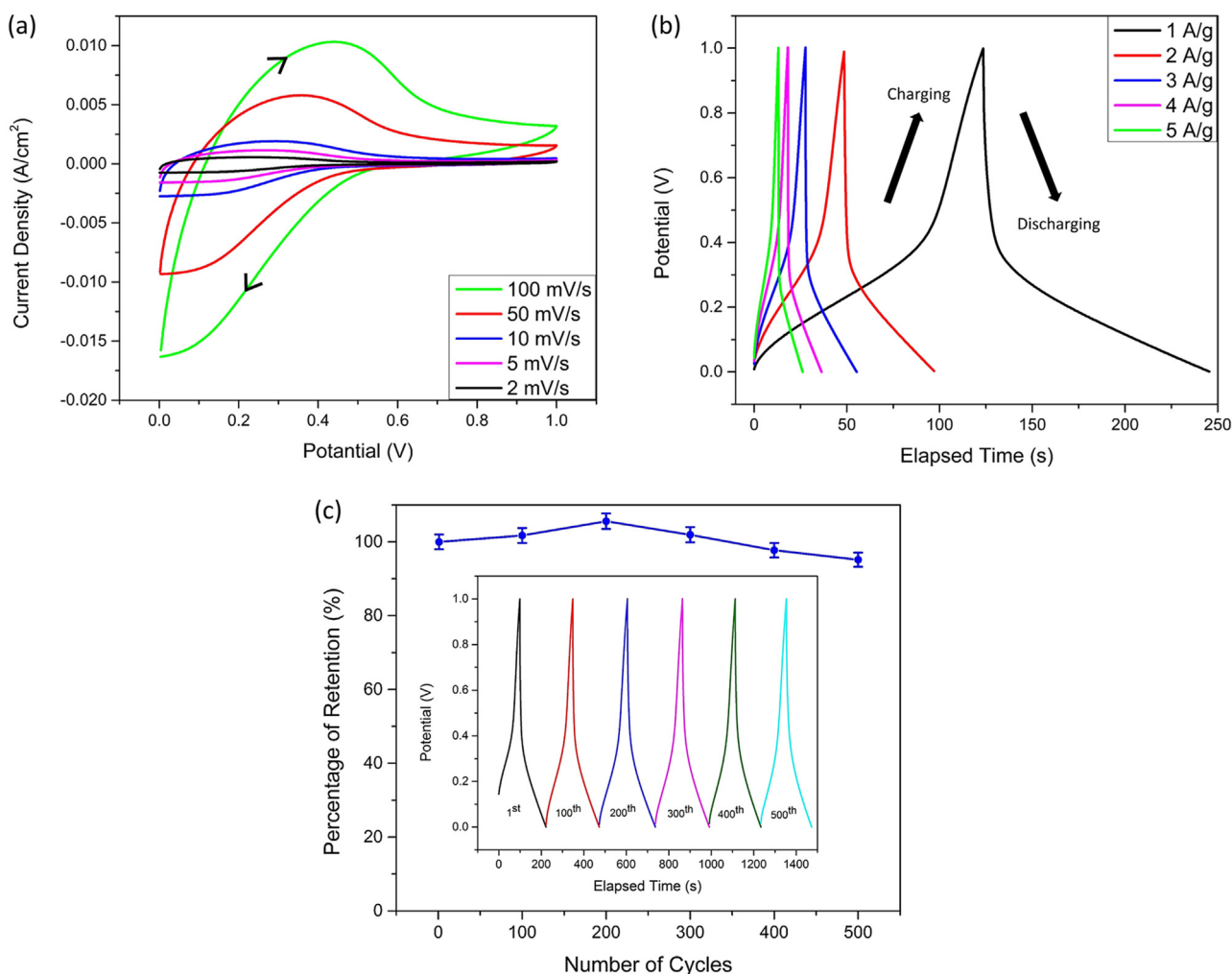
Fig. 3. Electrochemical characterization of PPy/rGO-based supercapacitor: (a) CV curves at different scan rates, (b) GCD curves at different current densities and (c) specific capacitance retention percentage at 500 GCD cycles at a current density of $1\,A\,g^{-1}$ with their respective curves shown in the inset.

From the EIS test, the Nyquist plot showed a straight line and an arc in the low-frequency and high-frequency regions, respectively (Fig. S3, Supplementary Information). The straight line indicated ion diffusion on the electrode surface [15]. If the slope of the line was greater, then the supercapacitor would be closer to an ideal capacitor. On the other hand, the arc at a high frequency was related to the electronic resistance between the graphene sheets [15]. The equivalent series resistance (ESR) and charge transfer resistance (Rct) values obtained from the Nyquist plot were 0.69 Ω and 4.2 Ω, respectively. Cyclic stability is a vital parameter for application purposes and feasibility measurements. A life stability test up to 500 cycles was conducted, and the retention percentages for groups of 100 cycles are plotted in Fig. 3(c). The specific capacitance increased from 272.9 F g^{-1} (1st cycle) to 288.2 F g^{-1} (200th cycle) before a slight decrease to 259.7 F g^{-1} at the 500th cycle. After 500 cycles, there was a 4.8% total capacitance loss, resulting in a 95.2% retention of specific capacitance at a current density of 1 A g^{-1}. This slight decrease in specific capacitance was due to the loss of active materials in the current collector because of expansion and contraction during the GCD test, which resulted in a partial blockage of the regular configuration [28,33].

The DSSC was then integrated with the PPy/rGO-based supercapacitor in a three-electrode configuration to fabricate the photo-supercapacitor. The current response of the integrated photo-supercapacitor is shown in Fig. 4. First, the two external electrodes of the photo-supercapacitor were connected to a potentiostat under open circuit conditions, without solar illumination. Then, the photo-supercapacitor was charged under solar illumination with an intensity of 100 mW cm^{-2}. The presence of light resulted in the rapid generation of an anodic photocurrent up to 2.2 mA cm^{-2} as in Fig. 4, which then decreased drastically to 0.8 mA cm^{-2}. This behavior was consistent with other reported data and was mainly due to the injection of photo-generated charges into the super-capacitor electrodes for charging [21,22,34]. As for discharge, when the solar illumination was switched off, the current immediately dropped to zero because no electrons were excited or generated. This current response proved that the charging process of the integrated photo-supercapacitor was indeed initiated from the light.

In addition, to prove the combined functions of solar energy conversion and electrical energy delivery of the integrated photo-supercapacitor, the integrated system was photocharged and then galvanostatically discharged in the dark at currents of 1 mA and 5 mA with a charging cut-off potential of 0.5 V (Fig. S4, Supplementary Information). The charging procedure was the same as that of the previous current response, while the discharging was conducted in the dark by connecting only the supercapacitor's electrodes. The potentials that resulted from the two discharging currents increased gradually during the photocharging process until they reached the cut-off potential as shown in Fig. S4. Once the light illumination was blocked for discharge, both potentials were maintained at 0.5 V, with slight decays as a result of the self-discharge. This maintenance signified the success of the photo-charging mechanism [2]. Based on a comparison of the two discharge currents, the potential profile of 5 mA exhibited a higher rate of photocharging and galvanostatic discharging than that of 1 mA, with a relatively symmetrical and triangular shape, which is characteristic of an ideal supercapacitor. Therefore, by using a discharging current of 5 mA, the aforementioned process was repeated for 50 cycles to investigate the cycle stability of the integrated device. The percentage of retention of the specific capacitance and the respective curves is shown in Fig. 5. The specific capacitance increased from 123.9 F g^{-1} (1st cycle) to 124.7 F g^{-1} (10th cycle) before gradually decreasing to 87.8 F g^{-1} at the 50th cycle. After 50 consecutive cycles, the integrated system was able to retain 70.9% of its initial value with a 29.1% loss of specific capacitance due to the diminishing of the iodolyte solution, which resulted in the degeneration of the ruthenium dye molecules. This was confirmed by a change in the photoanode color from pink to white. In addition, the decay in the specific capacitance could also be observed by the decrease in the curve areas as the number of cycles increased. It is noteworthy to mention that this device was not encapsulated but was still able to achieve a promising retention percentage of the specific capacitance with a low decay rate. Based on this simple and proof-of-concept device architecture, the integrated system was able to harvest solar energy and release it in dark conditions, which is the fundamental working principle of a photo-supercapacitor [12].

Thus far, only a few attempts have been reported at making photo-supercapacitors, as shown in Table 1. In 2010, a photo-supercapacitor using platinum as an intermediate electrode was reported where 80% of its initial capacitance was retained after 10 cycles [2]. The platinum electrode separated the titania-based DSSC and PProDOT-Et$_2$ polymer-based supercapacitor by forming a

Fig. 4. Current density as a function of time for the photocharging of the integrated photo-supercapacitor.
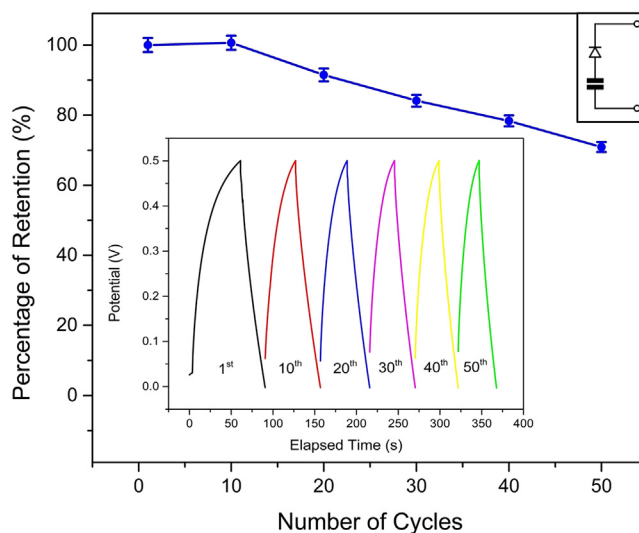
Fig. 5. Specific capacitance retention percentage of the photo-supercapacitor for 50 consecutive cycles at a current density of 5 mA/cm^2 with their respective photocharging/galvanostatic discharging curves showed in the inset. The corresponding circuit diagrams are shown in the top right inset.

Table 1
Comparison of previously-reported photo-supercapacitors compared to this work.

Interlayer	Solar cells			Supercapacitor (SC)	PCE (%)	$\eta_{overall}$ (%)	Retention	Ref
	Anode	Cathode	Substrate					
Pt sheet	TiO$_2$ nanoparticles	Pt sheet	FTO glass	Symmetric liquid SC based on PProDOT-Et$_2$	–	0.6	80% after 10 cycles	[2]
Pt sheet	TiO$_2$ particles	Pt sheet	ITO/PEN	Symmetric liquid SC based on PEDOT	4.4	–	–	[8]
Ag foil	TiO$_2$ with a TiO$_2$ blocking layer	Ag layer	FTO glass	Symmetric liquid SC based on RuO$_x$(OH)$_y$ on carbon paper	3.0	0.8	–	[21]
Si wafer	TiO$_2$ particles	carbonized porous silicon wafer	FTO glass	Symmetric solid SC based on carbonized porous silicon wafer	4.8	2.1	–	[12]
Ni foil	TiO$_2$ particles	PEDOT coated Ni foil	FTO glass	Asymmetric liquid SC based on active carbon and Ni(Co)O$_x$ on Ni foil	4.9	0.6	–	[22]
PEDOT-carbon	TiO$_2$ nanoparticles	PEDOT-carbon	FTO glass	Symmetric liquid SC based on PEDOT-carbon	6.4	4.7	96.8% after 50 cycles	[23]
Au film	ZnO nanorods (two cells)	Au	ITO/PET	Buckypaper-based SC	0.3	–	95.89% after 1000 cycles	[24]
PPy/rGO	TiO$_2$ nanoparticles with TiO$_2$ compact layer	PPy/rGO	ITO glass	Symmetric solid SC based on PPy/rGO on graphite sheet	2.4	–	70.9% after 50 cycles	This work

heterogeneous electrode. Subsequent works were conducted based on interlayers of silver foil [21], silicon wafer [12], and nickel foil [22] but no stability data was reported. In 2016, a photo-supercapacitor where a PEDOT-carbon electrode bridged the perovskite solar cell and a symmetric PEDOT-carbon-based supercapacitor was reported [23]. This interesting photo-super-capacitor based on the PEDOT-carbon interlayer was able to retain 96.8% of its initial capacitance after 50 life cycles. In this work, by replacing the interlayer with graphene, a charge retention of 70.9% was achieved after 50 life cycles, which was comparable to some of the previously reported works.

4. Conclusions

An integrated three-electrode photo-supercapacitor based on a dye-sensitized TiO$_2$ photoanode and a PPy/rGO symmetrical supercapacitor was fabricated using a simple deposition technique. In contrast with a conventional power conversion and energy storage device, this photo-supercapacitor was light-weight, utilized an easy fabrication technique, and showed promising energy storage behavior. After 50 consecutive charge/discharge cycles, this photo-supercapacitor was able to achieve a specific capacitance retention of 70.9% at a current density of 5 mA cm^{-2}, without utilizing any sealant. Unlike other attempts for integration, where individual materials like expensive platinum and other conductive nanomaterials were combined into a heterogeneous electrode as a bifunctional interlayer, our work employed graphene to act as the intermediate electrode for energy conversion and power storage. This simple and proof-of-concept device manifested the possibility of combining DSSC and supercapacitors. This work has also opened the door for the development of more effective self-powered electrochemical energy storage systems. By further optimizing the structure of the material and effective packaging of the integrated device, this novel photo-super-capacitor will be able to be a very promising renewable energy storage system in the near future.

Acknowledgements

Appendix A. Supplementary data

Supplementary data associated with this article can be found, in the online version, at http://dx.doi.org/10.1016/j.electacta.2017.04.003.

References

[1] J. Wang, X. Li, Y. Zi, S. Wang, Z. Li, L. Zheng, F. Yi, S. Li, Z.L. Wang, Adv. Mater. 27 (33) (2015) 4830–4836.
[2] C.-Y. Hsu, H.-W. Chen, K.-M. Lee, C.-W. Hu, K.-C. Ho, J. Power Sources 195 (2010) 6232–6238.
[3] J.D. Roy-Mayhew, G. Boschloo, A. Hagfeldt, I.A. Aksay, ACS applied materials & interfaces 4 (2012) 2794–2800.
[4] M.K. Nazeeruddin, R. Humphry-Baker, P. Liska, M. Grätzel, The Journal of Physical Chemistry B 107 (2003) 8981–8987.
[5] E. Palomares, J.N. Clifford, S.A. Haque, T. Lutz, J.R. Durrant, Chem. Commun. 14 (2002) 1464–1465.
[6] K.-M. Lee, V. Suryanarayanan, K.-C. Ho, Sol. Energy Mater. Sol. Cells 90 (2006) 2398–2404.
[7] M. Wang, Y. Wang, J. Li, Chem Commun. 47 (2011) 11246–11248.
[8] H.-W. Chen, C.-Y. Hsu, J.-G. Chen, K.-M. Lee, C.-C. Wang, K.-C. Huang, K.-C. Ho, J. Power Sources 195 (2010) 6225–6231.
[9] Y. Lee, M. Kang, Mater. Chem. Phys. 122 (2010) 284–289.
[10] D. Yu, X. Zhu, Z. Xu, X. Zhong, Q. Gui, Y. Song, S. Zhang, X. Chen, D. Li, ACS applied materials & interfaces 6 (2014) 8001–8005.
[11] C. Kim, S. Kim, J. Lee, K. Kim, J. Yoon, ACS applied materials & interfaces 7 (2015) 7486–7491.
[12] A.P. Cohn, W.R. Erwin, K. Share, L. Oakes, A.S. Westover, R.E. Carter, R. Bardhan, C.L. Pint, Nano Lett. 15 (2015) 2727–2731.
[13] X. Xia, Y. Zhang, D. Chao, Q. Xiong, Z. Fan, X. Tong, J. Tu, H. Zhang, H.J. Fan, Energy & Environmental Science 8 (2015) 1559–1568.
[14] L.L. Zhang, X. Zhao, Chem. Soc. Rev. 38 (2009) 2520–2531.
[15] C. Liu, Z. Yu, D. Neff, A. Zhamu, B.Z. Jang, Nano Lett. 10 (2010) 4863–4868.
[16] H. Peng, Fiber-shaped integrated device, Fiber-Shaped Energy Harvesting and Storage Devices, Springer, Berlin Heidelberg, 2015, pp. 179–197.
[17] D.A. Brownson, D.K. Kampouris, C.E. Banks, Chem. Soc. Rev. 41 (2012) 6944–6976.
[18] J. Xu, H. Wu, L. Lu, S.F. Leung, D. Chen, X. Chen, Z. Fan, G. Shen, D. Li, Adv. Funct. Mater. 24 (2014) 1840–1846.
[19] G. Wee, T. Salim, Y.M. Lam, S.G. Mhaisalkar, M. Srinivasan, Energy & Environmental Science 4 (2011) 413–416.
[20] B. Liu, B. Liu, X. Wang, X. Wu, W. Zhao, Z. Xu, D. Chen, G. Shen, Adv. Mater. 26 (2014) 4999–5004.
[21] M. Skunik-Nuckowska, K. Grzejszczyk, P.J. Kulesza, L. Yang, N. Vlachopoulos, L. Häggman, E. Johansson, A. Hagfeldt, J. Power Sources 234 (2013) 91–99.
[22] N. Bagheri, A. Aghaei, M.Y. Ghotbi, E. Marzbanrad, N. Vlachopoulos, L. Häggman, M. Wang, G. Boschloo, A. Hagfeldt, M. Skunik-Nuckowska, Electrochim. Acta 143 (2014) 390–397.
[23] J. Xu, Z. Ku, Y. Zhang, D. Chao, H.J. Fan, Advanced Materials Technologies 1 (2016).
[24] F.-W. Lee, C.-W. Ma, Y.-H. Lin, P.-C. Huang, Y.-L. Su, Y.-J. Yang, Sensors and Materials 28 (2016) 749–756.
[25] G. Xin, Y. Wang, X. Liu, J. Zhang, Y. Wang, J. Huang, J. Zang, Electrochim. Acta 167 (2015) 254–261.
[26] N. Huang, H. Lim, C.H. Chia, M.A. Yarmo, M. Muhamad, International journal of nanomedicine 6 (2011) 3443–3448.

[27] Y.S. Lim, H.N. Lim, S.P. Lim, N.M. Huang, RSC Advances 4 (2014) 56445–56454.
[28] S. Mondal, U. Rana, S. Malik, Chem. Commun. 51 (2015) 12365–12368.
[29] J. Chen, Z. Xia, H. Li, Q. Li, Y. Zhang, Electrochim. Acta 166 (2015) 174–182.
[30] C. Ng, H. Lim, Y. Lim, W. Chee, N. Huang, International Journal of Energy Research 39 (2015) 344–355.
[31] X. Zhao, B. Zheng, T. Huang, C. Gao, Nanoscale 7 (2015) 9399–9404.
[32] M. Zhou, Y. Deng, K. Liang, X. Liu, B. Wei, W. Hu, J. Electroanal. Chem. 742 (2015) 1–7.
[33] W.K. Chee, H.N. Lim, N.M. Huang, International Journal of Energy Research 39 (2015) 111–119.
[34] H.M. Shiri, M. Aghazadeh, J. Electrochem. Soc. 159 (2012) E132–E138.